Cancer Nanotechnology

RESEARCH Open Access

Dual-targeting nanomedicine achieves synergistic multimodal therapy for tumor

Weidong Zhang[1,2], Liang Dai[1], Na Wang[1], Yunhe Liu[3], Zining Hao[2], Yaqian He[2], Song Ni[3*], Yimin Wang[1*] and Dawei Gao[2*]

*Correspondence:
nisong168@sina.com;
drwangyimin@126.com;
dwgao@ysu.edu.cn

[1] The First Hospital of Qinhuangdao, Qinhuangdao 066004, China
[2] State Key Laboratory of Metastable Materials Science and Technology, Nano-Biotechnology Key Lab of Hebei Province, Applying Chemistry Key Lab of Hebei Province, Heavy Metal Deep-Remediation in Water and Resource Reuse Key Lab of Hebei, Yanshan University, Qinhuangdao 066004, China
[3] National Clinical Research Center for Cancer/Cancer Hospital, National Cancer Center, Chinese Academy of Medical Sciences and Peking Union Medical College, Beijing 100021, China

Abstract

Background: The poor targeting delivery efficiency and limited efficacy of single therapeutic approach have consistently posed significant challenges in tumor management.

Results: In this research, we have conceived and synthesized a dual-targeting nanodrug delivery system denoted as PDA-DEM-Fe_3O_4@M, which incorporates a polydopamine nanoparticle (PDA) with photothermal properties, diethyl maleate (DEM) as a chemotherapy agent accelerating tumor apoptosis, iron oxide nanoparticles (Fe_3O_4) eliciting magnetic targeting effects, and tumor cell membranes (M) contributing to homologous targeting capabilities. The synergistic effect of PDA-induced photothermal therapy and DEM-mediated chemotherapy has been demonstrated in this study to exert a robust inhibitory and cytotoxic influence on tumor cells. Additionally, the biocompatibility of this system has also been demonstrated.

Conclusions: Through the synergistic effects of PDA's photothermal therapy and DEM's chemotherapy, this system demonstrated excellent inhibition and killing effects on tumor cells. Furthermore, we established its excellent biological safety profile. This study demonstrated the potential of this nanomaterial for clinical application in tumor therapy.

Keywords: Tumor therapy, Targeting delivery, Photothermal therapy, Synergistic effect

Background

Tumors pose a serious threat to human life and health due to their high incidence and mortality rates (Siegel et al. 2023). In recent years, with the continuous advancement of nanobiotechnology, nanocarriers have been widely applied in the field of tumor therapy (Lin et al. 2023; Zhan et al. 2023; Li et al. 2023). For tumor treatment, nanomedicines need to meet two fundamental requirements: firstly, excellent tumor targeting ability, which is essential for ensuring the efficacy and biocompatibility of nanomedicines (Zeng et al. 2023); secondly, effective therapeutic strategies that differ from conventional single-modal chemotherapy and radiotherapy (Yang et al. 2023). Exploring novel combination therapies is a necessary condition to improve the anti-tumor efficacy of nanomedicines.

Regarding the tumor targeting issue of nanomedicines, there are mainly two approaches: passive targeting and active targeting. Passive targeting relies primarily on the enhanced permeability and retention (EPR) effect of nanomedicines, achieved by adjusting the nanoparticle size to facilitate their accumulation in the tumor region (Sun et al. 2022; Xu et al. 2023). However, the performance of the EPR effect varies significantly among different individuals, leading to suboptimal outcomes in passive targeting(Zi et al. 2022; Jeon et al. 2022). In contrast, active targeting offers diverse methods that take advantage of tumor-specific microenvironments, such as low pH and hypoxia, to achieve specific surface modifications of nanomedicines, thereby enabling active targeting accumulation (Visser and Joyce 2023; Cheng et al. 2022; Wan et al. 2023). Magnetic targeting, unlike other techniques, not only possesses strong tissue-penetrating capabilities but also has no impact on normal tissues, making it an ideal external stimulus (Ma et al. 2023a, b). Sun et al. utilized the vibrational properties of magnetic iron oxide nanoparticles in an alternating magnetic field to convert magnetic energy into thermal energy, thus achieving magnetic hyperthermia for tumor cell destruction (Sun et al. 2023). Additionally, in the preliminary research of our research group, iron oxide nanoparticles were combined with nanomedicines' surfaces, achieving active targeting aggregation at the tumor site under the control of an external magnetic field (Gao et al. 2020). Simultaneously, extensive research is dedicated to preparing cell membranes as biomimetic materials, endowing nanomedicines with complex functionalities such as ligand recognition targeting, immune evasion, and prolonged blood circulation, all crucial for effective drug delivery to tumor lesions (Miao et al. 2022; Pan et al. 2022; Chen et al. 2023a, b, c). For instance, employing the homologous targeting strategy, the cell membrane of the same tumor type was isolated and integrated onto the surface of nanomedicines, allowing them to evade recognition by macrophages during transportation in the body while retaining self-recognition ability for similar tumor cells, thereby improving the active tumor targeting efficiency of nanomedicines (Zhu et al. 2016; Bai et al. 2022).

In addition, addressing the issue of traditional chemotherapy/radiotherapy being single-modal and associated with significant toxic side effects, researchers have developed numerous novel therapeutic strategies in recent years. These strategies include photothermal therapy (Li et al. 2022a, b), photodynamic therapy (Zhu et al. 2022), immunotherapy (Chen et al. 2023a, b, c), and catalytic therapy (Fu et al. 2022), among others. Building upon these advancements, various treatment modalities have been combined to achieve synergistic effects in tumor therapy. In our previous research, our team integrated different therapeutic modalities, and compared to traditional single-modal chemotherapy/radiotherapy, the synergistic effect of multi-modal therapy significantly improved the therapeutic efficacy of nanomedicines while concurrently reducing their toxic side effects on normal tissues (He et al. 2022; Li et al. 2022a, b). In this process, we noted that Polydopamine (PDA), as a synthetically derived polymer, finds extensive applications in the field of drug delivery (Zhang et al. 2023; Qiu et al. 2023). PDA not only boasts a straightforward synthesis method but also exhibits excellent biocompatibility (Acter et al. 2023). Its remarkable self-assembly properties enable the formation of uniform and dense coatings on various surfaces, as well as the self-assembly into microsphere structures for drug encapsulation (Jiang et al. 2023; Chen et al. 2023a, b,

c). Additionally, PDA demonstrates excellent photothermal conversion capabilities, efficiently absorbing 808 nm near-infrared (NIR) light and converting it into heat for tumor photothermal therapy (Zhong et al. 2022).

In this study, we developed a dual-targeting nanomedicine, PDA-DEM-Fe_3O_4@M, which demonstrated a synergistic effect of photothermal therapy and chemotherapy. This nanosystem is composed of PDA with photothermal effects (Hsieh et al. 2022), diethyl maleate (DEM) as a chemotherapy drug to induce tumor apoptosis (Kang et al. 2023), iron oxide nanoparticles (Fe_3O_4) with magnetic targeting capability (Tao et al. 2022), and tumor cell membranes (M) with homologous targeting ability(Chi et al. 2022). Using PDA as the core, DEM was loaded through covalent binding and charge adsorption, while Fe_3O_4 nanoparticles and tumor cell membranes were conjugated to the outer layer. The dual-targeting effect mediated by Fe_3O_4 nanoparticles and the homologous targeting effect of tumor cell membranes enhanced the accumulation of the nanocarrier system at the tumor site. Under NIR light irradiation at 808 nm, the photothermal effect of activated PDA facilitated the release of DEM, achieving a synergistic effect of chemotherapy and photothermal therapy.

Materials

Preparation of PDA-DEM-Fe_3O_4@M

Weigh 15.5 mg of dopamine and place it into a 50 mL beaker. Add Tris-HCl solution (pH = 8.5) and then add 150 μL of diethyl maleate. Stir the mixture using a magnetic stirrer for 2 h at 3000 rpm. Centrifuge the mixture at 3000 rpm for 10 min, discard the precipitate, and collect the supernatant. Centrifuge the supernatant at 12,000 rpm for 10 min, discard the supernatant, and wash the precipitate with 1 mL of ultrapure water, repeating this process 3 times. Add the obtained precipitate to 10 mL of ultrapure water and sonicate for 5 min to obtain the PDA-DEM solution for further use.

Take 10 mL of the PDA-DEM solution and add 10 mg of Fe_3O_4 nanoparticles with a particle size of 20 nm. Stir the mixture mechanically for 1 h and then centrifuge it at 3000 rpm. Remove the precipitate to obtain the PDA-DEM-Fe_3O_4 nanoparticle solution.

Take HeLa cells, wash them 3 times with PBS by centrifugation (1500 rpm, 5 min each time). Resuspend the cells in 1 mL of deionized water in a 2 mL centrifuge tube. Swell the cells at 37 °C for 30 min, followed by ultrasonic disruption (parameters: power 300 W, on for 2 s, off for 2 s, total duration 10 min, ice bath to maintain temperature below 45 °C). After ultrasonic disruption, centrifuge at 3000 rpm for 10 min, discard the precipitate, and then centrifuge the upper solution at 13,000 rpm for 1 h. Discard the supernatant, add 1 mL of water, and sonicate for 15 min to obtain the disrupted HeLa cell membrane solution.

Mix the disrupted HeLa cell membrane solution with the PDA-DEM-Fe_3O_4 nanoparticle solution. Add the prepared mixture into a polycarbonate membrane extruder for 10 cycles of repeated extrusion. Finally, obtain PDA-DEM-Fe_3O_4@M.

Characterization

Draw the solution of the test sample and drop it onto a carbon support film, allowing the solution to air-dry at room temperature. Subsequently, observe the sample using a Hitachi HT7700 transmission electron microscope. Place the test sample solution in an

ultrasonic cleaner for 5 min to ensure uniform dispersion of the sample. Then, dilute the test sample solution 10 times and measure its particle size distribution and zeta potential using a Malvern laser particle size analyzer, Zetasizer Nano ZS90.

Photothermal performance

Take 500 μL of the test sample solution in a 1.5 mL centrifuge tube. Employ an 808 nm, 2 W/cm² near-infrared laser emitter to irradiate the test sample. Use a portable infrared thermal imaging camera (InfraTec VarioCAM) to measure and capture images of the solution's temperature. Record the temperature every 30 s during the irradiation process.

Antitumor effect in vitro

Add HeLa cells to a 96-well plate with 100 μL of solution per well, containing 5.0×10^4 cells per well. After incubating in a CO2 incubator for 24 h, add the test samples to the wells. Prior to addition, filter the samples through a 0.22 μm syringe filter for sterilization, and set up triplicate wells for each test sample. After a certain exposure time of the samples to HeLa cells, remove the original solution, add 200 μL of 0.5 mg/mL MTT solution to each well, and incubate for 4 hours in the incubator. Finally, discard the MTT solution, add 150 μL of DMSO to each well, vigorously mix, and place the 96-well plate in a multi-mode microplate reader (Molecular Devices M2e) to measure the absorbance at 540 nm wavelength. Calculate cell viability using Eq. (1):

$$\text{Cell viability (\%)} = \text{OD}_{\text{sample}} / \text{OD}_{\text{control}} \times 100 \tag{1}$$

Where $\text{OD}_{\text{sample}}$ is the average absorbance of the test sample wells and $\text{OD}_{\text{control}}$ is the average absorbance of the control wells (PBS).

Antitumor effect in vivo

The animal experiments conducted in this paper were carried out in accordance with the regulations of the Animal Ethics Committee of Yanshan University. Kunming mice were used for the experiments, and U14 cells were subcutaneously implanted into the right hind limb of the mice. Tumor-bearing mice were randomly divided into groups, with 6 mice in each group. The tumor volume of each mouse was measured daily using calipers. When the tumor volume reached 100 mm³, the drug treatment could be initiated. The tumor volume (V) of each mouse was calculated using Eq. (2):

$$V = ab^2/2 \tag{2}$$

Where "a" is the maximum diameter of the tumor, and "b" is the minimum diameter of the tumor.

The drug was administered via tail vein injection every other day, and specific groups received corresponding light exposure treatments according to the experimental requirements. In the magnetic field treatment group, a magnet was fixed at the tumor tissue of the mice to provide a stable magnetic field. The mice's weight and tumor volume changes were recorded every other day. After the completion of the drug treatment,

the mice were euthanized by cervical dislocation, and the serum levels of ALT, AST, and BUN indicators were detected using Elisa kits.

Statistical analysis

The obtained data are presented as mean ± standard error (SE). Statistical significance (*$p < 0.05$ or **$p < 0.01$) was evaluated using one-way analysis of variance (ANOVA). Data analysis plots were generated using Origin 8.5 software.

Result and discussion

Characterization

Figure 1A and C depict the TEM images of PDA-DEM, PDA-DEM-Fe_3O_4, and PDA-DEM- Fe_3O_4@M, respectively. From the images, it can be observed that the nanoparticles exhibit a spherical structure, and with the encapsulation of Fe_3O_4 and tumor cells, there is an increase in the size of the nanoparticles. This observation is consistent with the dynamic light scattering (DLS) results. The diameter of PDA-DEM is 51.2 ± 1.6 nm (Fig. 1D), PDA-DEM-Fe_3O_4 has a diameter of 103.3 ± 2.4 nm (Fig. 1E), and PDA-DEM-Fe_3O_4@M has a diameter of 110.6 ± 1.7 nm (Fig. 1F). Zeta potential results (Fig. 1G) show that pure PDA nanoparticles possess a negative surface charge (− 1.7 ± 0.7 mV).

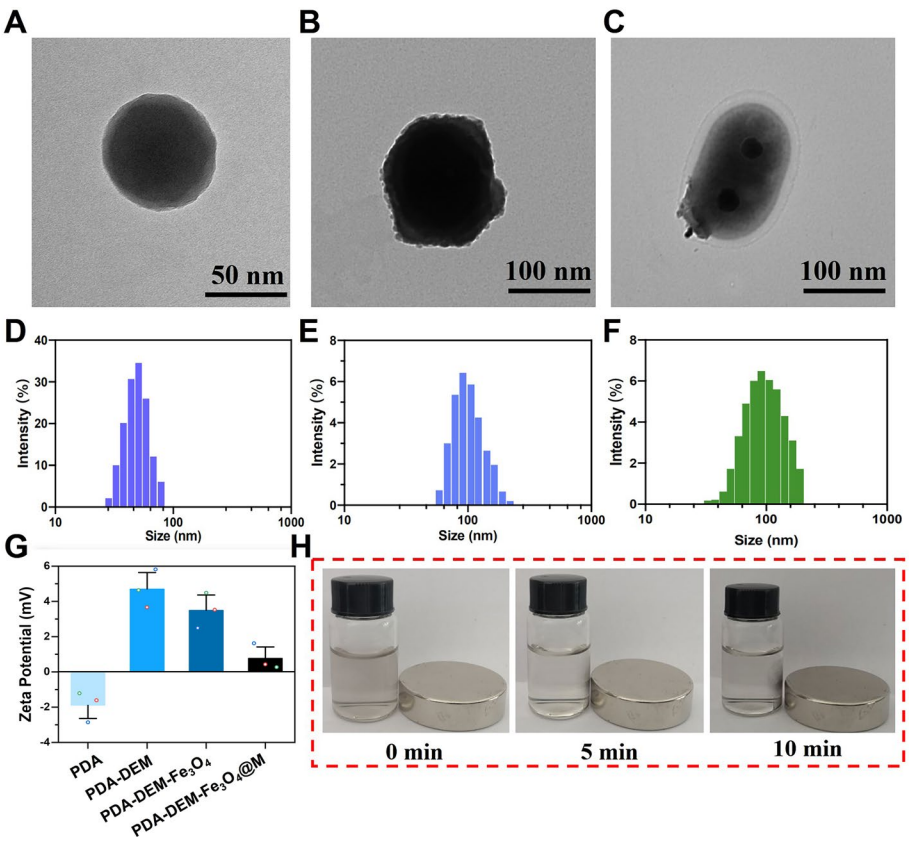

Fig. 1 Transmission electron microscope images of (**A**) PDA-DEM, (**B**) PDA-DEM- Fe_3O_4, (**C**) PDA-DEM-Fe_3O_4@M; Dynamic light scattering size analysis of (**D**) PDA-DEM, (**E**) PDA-DEM- Fe_3O_4, (**F**) PDA-DEM- Fe_3O_4@M; (**G**) Zate potential; (H) Magnetic characterization of PDA-DEM- Fe_3O_4@M

Upon loading with DEM and Fe_3O_4 nanoparticles, the surface charge becomes positive (4.5 ± 0.3 mV, 3.9 ± 0.4 mV). However, after the encapsulation of tumor cell membranes, the surface charge of the nanoparticles decreases due to the negative charge on the cell membrane surface (0.4 ± 0.1 mV).

Furthermore, we validated the magnetic responsiveness of PDA-DEM-Fe_3O_4@M, as shown in Fig. 1H. Over time, the nanoparticles gradually concentrate near the magnetically attracted sites, providing evidence for the excellent magnetic responsiveness of PDA-DEM-Fe_3O_4@M. We also attempted to characterize the nanoparticles using XRD, and the results are shown in Additional file 1: Fig S1. By comparing with the standard Fe_3O_4 card, it was confirmed that Fe_3O_4 is present in these nanoparticles. All these results collectively confirm the successful synthesis of PDA-DEM-Fe_3O_4@M.

Photothermal performance

Due to the excellent photothermal conversion performance of PDA, which can absorb near-infrared light and convert it into heat (Wu et al. 2023), we conducted photothermal performance characterization on PDA-based nanoparticles. As shown in Fig. 2A, under near-infrared light irradiation at a wavelength of 808 nm and a power of 2 W/cm², the nanoparticles exhibited effective temperature elevation due to the presence of PDA. After 10 min of irradiation, the temperatures of PDA, PDA-DEM, PDA-DEM Fe_3O_4, and PDA-DEM-Fe_3O_4@M increased to 44, 44.5, 45.5, and 48 °C, respectively. Since tumor cells are highly sensitive to temperature elevation, local temperatures reaching 42 °C are sufficient to induce tumor cell ablation (Yang et al. 2022). Therefore, the photothermal heating performance of PDA-DEM-Fe_3O_4@M fully meets the requirements of photothermal therapy. Moreover, we recorded images of the in vitro photothermal heating effect of PDA-DEM-Fe_3O_4@M using a thermal imaging camera, as shown in Fig. 2B, which is consistent with the photothermal heating curve. These results collectively demonstrate the excellent photothermal conversion performance of PDA-DEM-Fe_3O_4@M.

Antitumor effect in vitro

To demonstrate the in vitro anti-tumor effect of PDA-DEM- Fe_3O_4@M, we treated HeLa cells with different nanoparticles and analyzed the tumor cell inhibition rate using the MTT assay, as shown in Fig. 3A. PDA-DEM and PDA-DEM-Fe_3O_4 exhibited similar inhibitory effects on HeLa cells, with cell viabilities of 90 and 88.32%,

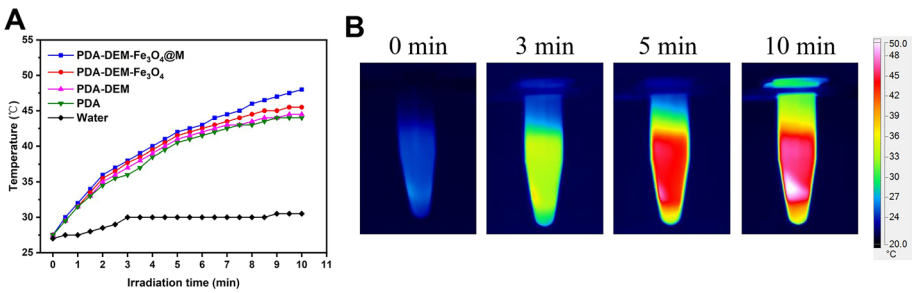

Fig. 2 **A** Temperature changes of different samples, **B** Thermal images of PDA-DEM-Fe_3O_4@M with laser irradiation

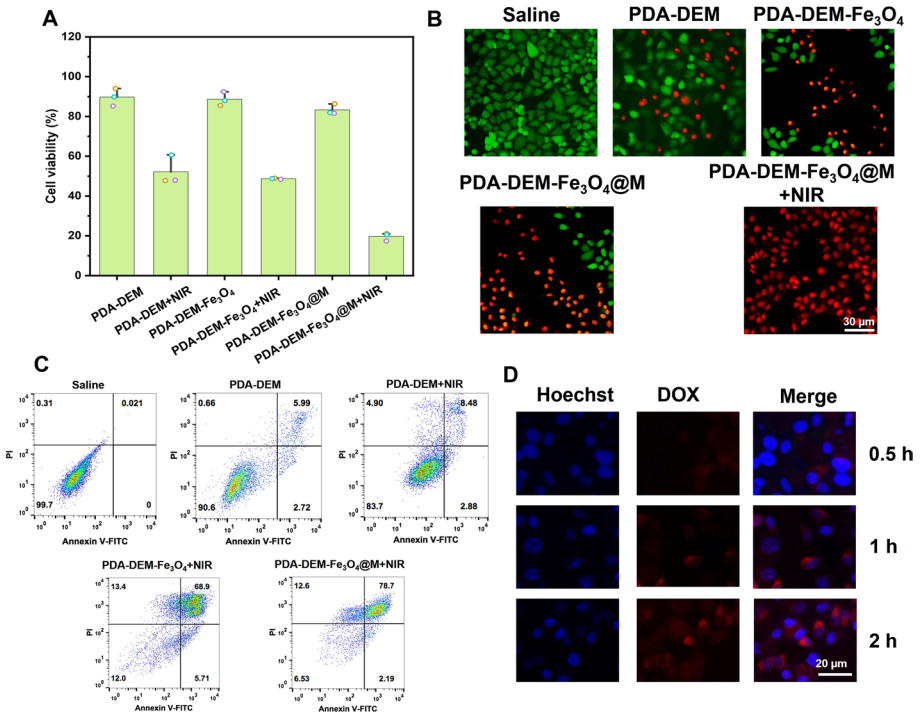

Fig. 3 (**A**) Cell viability of HeLa cells under different treatment conditions; (**B**) Fluorescence images of live/dead staining of HeLa cells; (**C**) Cell apoptosis of HeLa cells under different treatment conditions; (**D**) Uptake of PDA-DOX-Fe_3O_4@M by HeLa cells at different treatment times

respectively. However, due to the tumor cell membrane encapsulation and the homologous targeting effect, PDA-DEM-Fe_3O_4@M showed enhanced accumulation within HeLa cells, resulting in improved inhibition with a cell viability of 81.92%. The PDA-DEM + NIR and PDA-DEM-Fe_3O_4 + NIR groups, benefiting from their excellent photothermal conversion performance, promoted the release of DEM inside the cells and directly induced cell death through photothermal effects. Consequently, the cell viabilities of these groups were significantly reduced to 54.03 and 48.16%, respectively. In contrast, the PDA-DEM-Fe_3O_4@M + NIR group, benefiting from the combined effects of targeting, photothermal therapy, and chemotherapy, exhibited the most pronounced tumor cell inhibition, with a cell viability of only 19.21%. Figure 3B presents the live/dead staining results for HeLa cells under different treatments. Compared to other groups, the PDA-DEM-Fe_3O_4@M + NIR group had the highest amount of dead cells (red), confirming the potent tumor cell inhibition effect of PDA-DEM-Fe_3O_4@M under near-infrared light irradiation. In Fig. 3C, the apoptosis assay demonstrated varying levels of tumor cell apoptosis under different treatments. The PDA-DEM group primarily relied on the chemotherapy effect of DEM, resulting in a limited apoptosis rate. However, the cell apoptosis rates of PDA-DEM and PDA-DEM-Fe_3O_4 significantly increased under near-infrared light stimulation. The PDA-DEM-Fe_3O_4@M + NIR group, benefiting from the synergistic effect of photothermal therapy and chemotherapy, as well as the targeting effect of the cell membrane, exhibited substantial tumor cell apoptosis, consistent with the MTT assay results.

Cellular uptake

Furthermore, we investigated the cellular uptake capacity of HeLa cells for PDA-DEM-Fe_3O_4@M. To replace DEM with a model drug, we used DOX, which possesses fluorescent properties. The results, as shown in Fig. 3D, revealed that the red fluorescence within HeLa cells gradually intensified with increasing incubation time. Similar experimental results were observed in flow cytometry analysis (Additional file 1: Fig S2). This indicates a growing accumulation of nanoparticles within tumor cells, facilitated by the encapsulation of the nanoparticles with the tumor cell membrane. Studies suggest that cells from the same origin exhibit excellent targeting effects (Ma et al. 2023a, b). Leveraging this principle, by coating nanoparticles with tumor cell membranes from the same source, the targeting delivery efficiency can be significantly improved. This not only enhances the delivery efficiency of nanoparticles and drugs but also reduces their toxic side effects on normal tissues.

Antitumor effect in vivo

Due to the use of U14 cells in animal experiments, the cell membrane wrapped around the nanoparticle surface was replaced with the U14 cell membrane to achieve homologous targeting effects in animal experiments. We first characterized the photothermal therapy effect of PDA-DEM-Fe_3O_4@M in mice, as shown in Fig. 4A. Compared to the saline control group, the PDA-DEM-Fe_3O_4@M-treated group exhibited a significant increase in local tumor temperature upon exposure to 808 nm near-infrared light. After 10 min of irradiation, the temperature rose to 45 °C, reaching the temperature required for tumor cell ablation, thus achieving the effect of tumor photothermal therapy. Subsequently, we observed the changes in body weight of mice in different treatment groups,

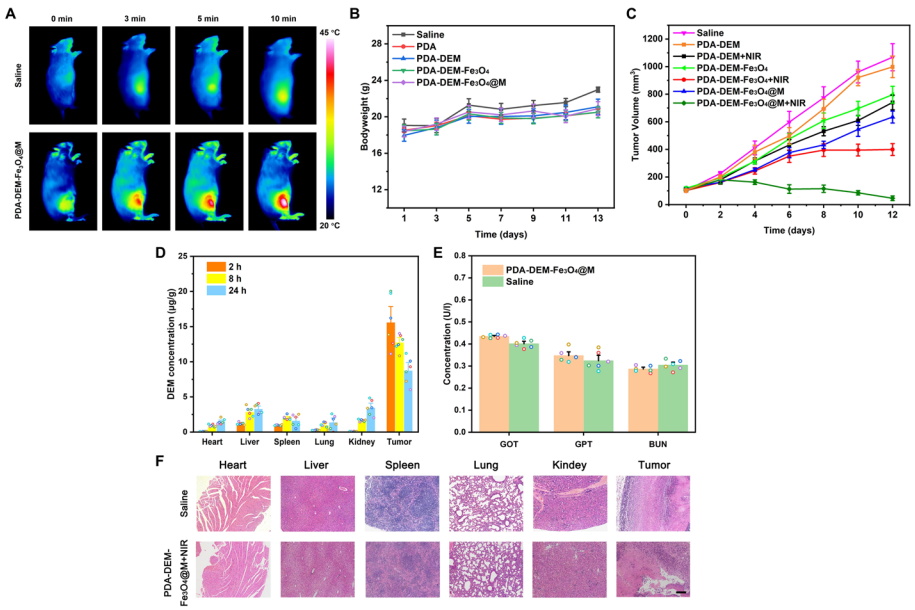

Fig. 4 **A** Infrared thermal imaging of tumor-bearing mice injected with PDA-DEM-Fe_3O_4@M and subjected to near-infrared light irradiation; **B** Body weight change curve; **C** Tumor volume change curve in mice under different treatment conditions; **D** Distribution of DEM in mice. **E** Detection of liver and kidney indicators ALT, AST, and BUN in mice. **F** HE-stained images of various tissues in mice. Scale bar: 100 μm

as depicted in Fig. 4B. During the treatment period, there was no significant change in the body weight of mice in the various treatment groups compared to the blank control group, indicating that the drug treatment did not significantly affect the health of the mice.

Figure 4C shows the changes in tumor volume among different treatment groups. From the graph, it can be observed that the PDA-DEM-Fe_3O_4@M + NIR group exhibited the most significant tumor inhibition effect compared to other treatment groups. This can be attributed to the following two factors. Firstly, guided by the homologous targeting of the tumor cell membrane and the external magnetic field-guided tumor local targeting of Fe_3O_4 nanoparticles, the PDA-DEM-Fe_3O_4@M nanoparticles accumulated effectively in the tumor tissue. Secondly, under external near-infrared light irradiation, PDA could convert absorbed light energy into heat, exerting a photothermal therapy effect on tumor cells. Simultaneously, the release of DEM at the tumor site accelerated tumor cell apoptosis. With the synergistic effect of chemotherapy and photothermal therapy, PDA-DEM-Fe_3O_4@M demonstrated a strong in vivo anti-tumor effect.

Biological safety

We investigated the distribution of nanoparticles in mice. The results, as shown in Fig. 4D, indicate that after intravenous injection of nanoparticles, there was a noticeable accumulation of the drug at the tumor site over time compared to other tissues. Subsequently, due to metabolic processes, the drug content at the tumor site gradually decreases and undergoes metabolism in the liver and kidneys. In addition, we conducted serum biochemical tests for liver function markers (ALT and AST) and kidney function marker (BUN) on mice in the Saline group and the PDA-DEM-Fe_3O_4@M group to further assess whether PDA-DEM-Fe_3O_4@M has an impact on normal physiological functions. As shown in Fig. 4E, the levels of ALT, AST, and BUN in the serum were measured. ALT and AST are primary parameters for evaluating liver function, and their levels significantly increase when the liver is damaged. BUN is a marker of kidney function, and elevated BUN levels indicate kidney impairment(Luo et al. 2022). Comparative analysis revealed no significant differences between the Saline group and the PDA-DEM-Fe_3O_4@M group. This result indicates that PDA-DEM-Fe_3O_4@M has no significant impact on liver and kidney functions in mice and demonstrates good biological safety. We also performed tissue sectioning and HE staining. The results, as shown in Fig. 4F, indicate that the treatment with nanoparticles did not cause significant damage to the main organs of the mice. However, it demonstrated a noticeable destructive effect on the tumor tissue. As a nanomedicine delivery system, PDA-DEM-Fe_3O_4@M shows relative safety and reliability, suggesting promising prospects for clinical applications.

Conclusion

In this study, we designed and synthesized a dual-targeting nanomedicine delivery system, PDA-DEM-Fe_3O_4@M, which combines magnetic and homologous tumor cell membrane targeting. Through the synergistic effects of PDA's photothermal therapy and DEM's chemotherapy, this system demonstrated excellent inhibition and killing effects on tumor cells. These effects were effectively validated through both in vitro and in vivo anti-tumor experiments. Furthermore, by assessing the liver and kidney indicators of

mice treated with PDA-DEM-Fe_3O_4@M, we established its robust biological safety profile. This finding also underscores the potential of this nanomaterial for clinical application in tumor therapy.

Supplementary Information

The online version contains supplementary material available at https://doi.org/10.1186/s12645-023-00244-0.

Author contributions
WZ, SN, YW and DG made substantial contributions to the conception and design of the work. WZ was responsible for sample preparation, characterization and article writing. LD and NW were responsible for the cell experiments. ZH and YH were responsible for the animal experiments. All authors read and approved the final manuscript.

Funding
This work was supported by Joint Fund Project of National Natural Science Foundation of China (U21A20309), National Natural Science Foundation (No. 22078280, 22108235, 22208282, 21776238), Natural Science Foundation of Hebei Province (No. B2020203034), Natural Science Foundation of Hebei Province (No.H2020107010), Postdoctoral Science Foundation of Hebei Province (No. B2021003046) and Featured special cultivation projects (No. UY202202).

Availability of data and materials
The datasets used and/or analysed during the current study are available from the corresponding author on reasonable request.

Declarations

Ethics approval and consent to participate
No human participants, human data or human tissue were involved in this study. No any individual person's data was involved in this study.

Competing interests
The authors declare no competing interests.

Received: 14 September 2023 Accepted: 27 December 2023
Published online: 13 January 2024

References

Acter S et al (2023) Polydopamine nanomaterials for overcoming current challenges in cancer treatment. Nanomaterials (Basel) 13(10):1656
Bai XF et al (2022) Homotypic targeted photosensitive nanointerferer for tumor cell cycle arrest to boost tumor photoimmunotherapy. ACS Nano 16(11):18555–18567
Chen J et al (2023) Targeted therapy of oral squamous cell carcinoma with cancer cell membrane coated co-fc nanoparticles via autophagy inhibition. Adv Funct Mater 33(24):2300235
Chen W et al (2023) In situ engineering of tumor-associated macrophages via a nanodrug-delivering-drug (beta-Elemene@Stanene) strategy for enhanced cancer chemo-immunotherapy. Angew Chem Int Ed Engl 62:e202308413
Chen A et al (2023) Zwitterionic polymer/polydopamine coating of electrode arrays reduces fibrosis and residual hearing loss after cochlear implantation. Adv Healthc Mater 12(1):e2200807
Cheng R et al (2022) A pH-responsive cluster metal-organic framework nanoparticle for enhanced tumor accumulation and antitumor effect. Adv Mater 34(42):e2203915
Chi S et al (2022) Loading drugs in natural phospholipid bilayers of cell membrane shells to construct biomimetic nanocomposites for enhanced tumor therapy. ACS Appl Mater Interfaces 14(25):28671–28682
de Visser KE, Joyce JA (2023) The evolving tumor microenvironment: from cancer initiation to metastatic outgrowth. Cancer Cell 41(3):374–403
Fu Y et al (2022) Decrease in tumor interstitial pressure for enhanced drug intratumoral delivery and synergistic tumor therapy. ACS Nano 16(11):18376–18389
Gao W et al (2020) Nano magnetic liposomes-encapsulated parthenolide and glucose oxidase for ultra-efficient synergistic antitumor therapy. Nanotechnology 31(35):355104
He Y et al (2022) MoS(2) nanoflower-mediated enhanced intratumoral penetration and piezoelectric catalytic therapy. Biomaterials 290:121816
Hsieh M-H et al (2022) Tumor site-specific PEG detachment and active tumor homing of therapeutic PEGylated chitosan/folate-decorated polydopamine nanoparticles to augment antitumor efficacy of photothermal/chemo combination therapy. Chem Eng J 446:137243
Jeon S et al (2022) Prediction the clinical EPR effect of nanoparticles in patient-derived xenograft models. J Control Release 351:37–49
Jiang X et al (2023) Fabrication and properties of multi-functional polydopamine coated Cu/F-codoped hydroxyapatite hollow microspheres as drug carriers. Colloids Surf B Biointerfaces 222:113097
Kang N et al (2023) Stimuli-responsive ferroptosis for cancer therapy. Chem Soc Rev 52(12):3955–3972

Li X et al (2022) Reversing insufficient photothermal therapy-induced tumor relapse and metastasis by regulating cancer-associated fibroblasts. Nat Commun 13(1):2794
Li Z et al (2022) Downregulation of the tumor interstitial fluid pressure to boost intratumoral penetration and hydrodynamic therapy via CaO2-based Ru nanozymes. ACS Sustain Chem Eng 10(29):9506–9514
Li X et al (2023) Impairing tumor metabolic plasticity via a stable metal-phenolic-based polymeric nanomedicine to suppress colorectal cancer. Adv Mater 35(23):e2300548
Lin Y et al (2023) Radiotherapy-mediated redox homeostasis-controllable nanomedicine for enhanced ferroptosis sensitivity in tumor therapy. Acta Biomater 159:300–311
Luo Y et al (2022) IL-12 nanochaperone-engineered CAR T cell for robust tumor-immunotherapy. Biomaterials 281:121341
Ma J et al (2023) Tumor microenvironment targeting system for glioma treatment via fusion cell membrane coating nanotechnology. Biomaterials 295:122026
Ma X et al (2023) Modular-designed engineered bacteria for precision tumor immunotherapy via spatiotemporal manipulation by magnetic field. Nat Commun 14(1):1606
Miao Y et al (2022) Cell membrane-camouflaged nanocarriers with biomimetic deformability of erythrocytes for ultralong circulation and enhanced cancer therapy. ACS Nano 16(4):6527–6540
Pan WL et al (2022) Microenvironment-driven sequential ferroptosis, photodynamic therapy, and chemotherapy for targeted Breast cancer therapy by a cancer-cell-membrane-coated nanoscale metal-organic framework. Biomaterials 283:121449
Qiu H et al (2023) Hyaluronic acid-conjugated fluorescent probe-shielded polydopamine nanomedicines for targeted imaging and chemotherapy of bladder cancer. ACS Appl Mater Interfaces 15(40):46668–46680
Siegel RL et al (2023) Cancer statistics, 2023. CA Cancer J Clin 73(1):17–48
Sun R et al (2022) The tumor EPR effect for cancer drug delivery: current status, limitations, and alternatives. Adv Drug Deliv Rev 191:114614
Sun R et al (2023) Composite scaffolds of gelatin and Fe(3) O(4) nanoparticles for magnetic hyperthermia-based breast cancer treatment and adipose tissue regeneration. Adv Healthc Mater 12(9):e2202604
Tao Y et al (2022) Fe3O4 nanoparticles embedded in pectin–doxorubicin composites as pH-responsive nanoplatforms for tumor diagnosis and therapy by T1-weighted magnetic imaging. ACS Appl Nano Mater 6(1):633–645
Wan J et al (2023) Biodegradable NIR-II pseudo conjugate polymeric nanoparticles amplify photodynamic immunotherapy via alleviation of tumor hypoxia and tumor-associated macrophage reprogramming. Adv Mater 35(31):e2209799
Wu Y et al (2023) Near-infrared photothermal effect enhanced heterogeneous catalysis of Co3O4/PDA composite for highly efficient activation of peroxymonosulfate to degrade antibiotic pollutants. Chem Eng J 474:145267
Xu L et al (2023) Quantitative comparison of gold nanoparticle delivery via the enhanced permeation and retention (EPR) effect and mesenchymal stem cell (MSC)-based targeting. ACS Nano 17(3):2039–2052
Yang X et al (2022) Biomimetic aggregation-induced emission nanodots with hitchhiking function for T cell-mediated cancer targeting and NIR-II fluorescence-guided mild-temperature photothermal therapy. Adv Funct Mater 32(45):2206346
Yang T et al (2023) Mild chemo-photothermal synergistic therapy for tumors based on gold-nanoparticles coupled with metformin. ACS Appl Nano Mater 6(7):5729–5736
Zeng X et al (2023) Reduction/pH-responsive disassemblable MOF-microbial nanohybrid for targeted tumor penetration and synergistic therapy. Chem Eng J 452:13951
Zhan M et al (2023) Phosphorous dendron micelles as a nanomedicine platform for cooperative tumor chemoimmunotherapy via synergistic modulation of immune cells. Adv Mater 35(3):e2208277
Zhang Y et al (2023) Tumor-targeting gene-photothermal synergistic therapies based on multifunctional polydopamine nanoparticles. Chem Eng J 457:14131
Zhong W et al (2022) NIR-responsive polydopamine-based calcium carbonate hybrid nanoparticles delivering artesunate for cancer chemo-photothermal therapy. Acta Biomater 145:135–145
Zhu JY et al (2016) Preferential cancer cell self-recognition and tumor self-targeting by coating nanoparticles with homotypic cancer cell membranes. Nano Lett 16(9):5895–5901
Zhu D et al (2022) Tumor-derived exosomes co-delivering aggregation-induced emission luminogens and proton pump inhibitors for tumor glutamine starvation therapy and enhanced type-I photodynamic therapy. Biomaterials 283:121462
Zi Y et al (2022) Strategies to enhance drug delivery to solid tumors by harnessing the EPR effects and alternative targeting mechanisms. Adv Drug Deliv Rev 188:114449

Publisher's Note